Langmuir

Article

pubs.acs.org/Langmuir

Simulating the Formation of Surfactant-Templated Mesoporous Silica Materials: A Model with Both Surfactant Self-Assembly and Silica Polymerization

Lin Jin,[†] Scott M. Auerbach,*[,‡] and Peter A. Monson*[,†]

[†]Department of Chemical Engineering, University of Massachusetts, Amherst, 01003, Massachusetts, United States

[‡]Department of Chemistry, University of Massachusetts, Amherst, Massachusetts, 01003, United States

ABSTRACT: We have used Monte Carlo simulations to study the formation of the MCM-41 mesoporous silica material, with a new lattice model featuring explicit representations of both silicic acid condensation and surfactant self-assembly. Inspired by experimental syntheses, we have adopted the following two-step "synthesis" during our simulations: (i) high pH and low temperature allowing the initial onset of mesostructures with long-range order; (ii) lower pH and higher temperature promoting irreversible silica condensation. During step (i), the precursor solution was found to spontaneously separate into a surfactant−silicate-rich phase in equilibrium with a solvent-rich phase. Lamellar and hexagonal ordering emerged for the surfactant−silicate-rich mesosphases under different synthesis conditions, consistent with experimental observations. Under conditions where silica polymerization can be neglected, our simulations were found to transform reversibly between hexagonal and lamellar phases by changing temperature. During step (*ii*), silica polymerization was simulated at lower pH using reaction ensemble Monte Carlo to treat the pH dependence of silica deprotonation equilibria. Monte Carlo simulations produced silica−surfactant mesostructures with hexagonal arrays of pores and amorphous silica walls, exhibiting Q_n distributions in reasonable agreement with ^{29}Si NMR experiments on MCM-41. Compared with bulk amorphous silica, the wall domains of these simulated MCM-41 materials are characterized by even less order, larger fractions of 3- and 4-membered rings, and wider ring-size distributions.

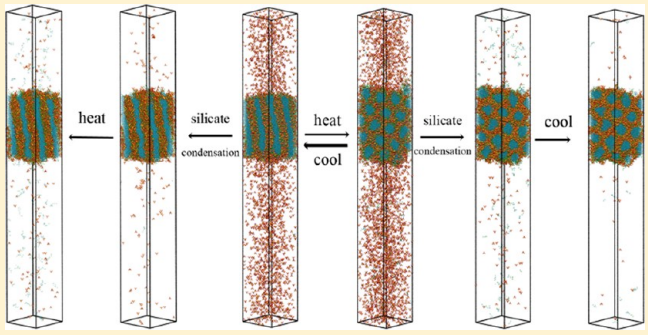

INTRODUCTION

Ordered mesoporous silica materials have been studied extensively since their discovery two decades ago[1−3] because of their potential applications in catalysis and separations of species too large to fit in zeolite micropores. Mesoporous silica materials have also been applied in biotechnology as bioadsorbents and biocatalysts,[4] and as drug delivery vehicles.[5,6] Tremendous effort has been made to understand their formation mechanism and to develop new materials with advanced functionalities.[7−22] Although progress has been made primarily through trial-and-error experimentation, the amorphous atomic structure and formation mechanism of MCM-41 remain poorly understood.[3] Molecular modeling has the potential to provide microscopic insights into these issues, and may offer design principles for controlling pore size, wall structure, surface morphology, and defects in mesoporous silica materials. In the present paper, we have developed and applied a composite model of silica and surfactant that produces atomic-level information on MCM-41 formation and structure.

MCM-41 can be synthesized with a variety of silica and alumina sources, different surfactant-to-silica ratios, under acidic or basic conditions, and over broad ranges of reaction times and temperatures.[15] In this paper, we focus on modeling alkaline solution syntheses of all-silica MCM-41 using alkyl-trimethylammonium $C_nH_{2n+1}(CH_3)_3N−OH/−Br$ as the structure-directing agent. One particular alkaline synthesis involves two main steps: the first begins with aqueous sodium silicate stirred for 10 min, followed by addition of surfactant solutions.[3] The resulting gel is stirred at room temperature for another 30 min. In the second main step, the system is then heated at 100 °C for 6 days. The resulting solids are recovered by filtration, washed in water, and dried in air. The as-synthesized product is then calcined at 540 °C to remove surfactant species and hence to empty the mesopores. The final calcination step also allows further silica condensation, thereby increasing the degree of polymerization. Pore sizes of 20−120 Å can be achieved, with typical pores of 40 Å and μm particle size.[15] Despite two decades of research into mesoporous silica materials, no microscopic model has shown how this two-step synthesis works, and more important, why it is needed.

To explain the formation of MCM-41, Beck et al. proposed a liquid-crystal (LC) templating mechanism.[3] They proposed that surfactant LC mesostructures serve as organic templates, around which silica condenses to form the MCM-41 structure. Beck et al. studied the formation of mesoporous materials using

Received: November 9, 2012
Published: December 5, 2012

surfactant molecules $C_nH_{2n+1}(CH_3)_3N-OH/-Br$ with different alkyl chain lengths (n = 6, 8, 10, 12, 14, and 16) and over synthesis temperatures ranging from 100 to 200 °C.[10] In the case of solutions containing the shortest alkyl chain surfactant (n = 6), only amorphous or zeolitic materials were formed over the entire temperature range examined, whereas using surfactants with longer chains (n = 8, 10, ..., 16) produced MCM-41 with various pore diameters, suggesting that hydrophobic interactions among surfactant tails play an important role during the formation of MCM-41. They also showed that, at 200 °C, only zeolitic and dense-phase products are obtained, probably due to the fast condensation of inorganic species that may hinder the longer-range ordering of pores in mesostructured materials. Crucial to the LC templating mechanism proposed by Beck et al. is the assumption that the hexagonal LC phase (denoted H_1) preforms from surfactant species under the synthesis conditions that produce MCM-41. However, this assumption was not experimentally tested in the work of Beck et al.[3,10]

Beck et al. also mentioned an alternate possible mechanistic pathway called cooperative templating where the silicate anion initiated the formation of liquid-crystal structure.[3] This possibility was investigated in detail by Davis and co-workers.[9] In particular, Chen et al. carried out *in situ* ^{14}N NMR spectroscopy, using this quadrupolar NMR method to search for the signature of a surfactant-generated H_1 phase. They found no NMR evidence of such a surfactant-generated H_1 phase at any time during the formation, and concluded that MCM-41 indeed forms by the cooperative templating mechanism. Chen et al. proposed that randomly rod-like micelles interact with silicate anions to approach charge balance and drive initial long-range ordering of these composite silicate−surfactant nanoparticles. Subsequent heating to promote silica condensation would then form MCM-41 from this semiordered, precursor nanoparticle phase. Davis and co-workers also suggested that the charge-compensating interactions between silicate anions and surfactant cations would preclude complete silica condensation.[9] Indeed, their ^{29}Si NMR results give $Q_2/Q_3/Q_4$ ratios of 7.5:55.7:36.8 and 4.6:52.2:43.2 for as-synthesized materials heated for 40 min and 20 h, respectively, where Q_n is the fraction of silicate species $Si(OSi)_n(OH)_{4-n}$ connected to n bridging oxygen atoms. Their XRD and ^{14}N NMR data revealed that condensation of silanol groups occurs over relatively long times—well after long-range order appears.

Monnier et al.[7] suggested a mechanism involving three processes during the formation of surfactant−silicate mesophases: (i) multidentate binding of silicate oligomers to the surface of preformed surfactant micelles, (ii) preferred polymerization of silicates at the surfactant−silicate interfaces, and (iii) charge density matching between silicates and surfactants. Their "cooperative formation" concepts were later investigated by Huo et al.,[23] who were able to organize inorganic molecular species into a variety of periodic mesostructures over a wide range of conditions. Their syntheses were inspired by the concepts of charge-density matching and multidentate binding between surfactants and inorganic species. These authors also suggested that silicate polyanions (e.g., dimers, double-three rings, and double-four rings) may interact preferentially with free surfactant molecules; in this scenario, surfactant micelles serve as a source of such free surfactants. Whether silicate anions interact preferentially with free surfactants or with surfactant micelles remains a controversial subject, as discussed below.

Later, Firouzi et al. used NMR, small-angle X-ray scattering, and polarized optical microscopy to study the precursor silicate−surfactant solutions that lead to MCM-41.[12] They observed reversible lamellar-to-hexagonal transitions of the composite silicate−surfactant system by adjusting temperature, under conditions of high pH (12−14) at which rates of silica condensation are strongly suppressed.[14] Precursor silicate−surfactant mesostructures with long-range order were found even at extremely low surfactant concentrations (e.g., 1 wt %), low enough to be in the micellar region of the cetyltrimethylammonium bromide (CTABr)/water binary phase diagram,[24] providing additional evidence of cooperative templating. In particular, Firouzi et al. reported that a 25-to-60 °C step change caused a lamellar-to-hexagonal transition within 0.3 h, whereas the reverse 60-to-25 °C step produced the reverse hexagonal-to-lamellar phase change over 4 h. Siperstein and Gubbins reported lattice Monte Carlo studies (*vide infra*) of this ternary silicate−surfactant−solvent system, showing collective lamellar and hexagonal phases.[25,26] However, the reversibility of the lamellar-to-hexagonal transition has yet to be reproduced by simulation.

Firouzi et al. also introduced alternative ideas for "turning on" silica condensation;[14] these ideas were later studied in detail by Lin and Mou.[20] They compared heating at high pH to dropping the pH from 11 to 12 to 8−9, finding that such "delayed neutralization" produced MCM-41 samples with more complete silica condensation and thicker silica walls.[20] Below, we study this effect by treating the pH dependence of silica condensation with the reaction ensemble Monte Carlo method.[27,28]

These seminal experiments and subsequent ones have generally found that the formation of MCM-41 starts with a relatively rapid evolution to a hexagonal mesophase with long-range order, followed by a slower process of silicate condensation within the inorganic phase. Zhang et al.[29] carried out *in situ* electron paramagnetic resonance (EPR) spectroscopy and identified two stages during formation of hexagonal MCM-41: hexagonal long-range order formed in 5−8 min, followed by slower silicate condensation reactions indicated by the slow-down of the spin probe motion (>1.5 h). Using *in situ* small-angle X-ray scattering, Linden and co-workers[30,31] studied the initial stages of formation of MCM-41 and observed that the hexagonal mesophase formed within 3 min of the reaction without passing through any intermediate phase, and the solid product obtained after 3 min was only partially condensed.

Despite this broad agreement on the cooperative templating mechanism and the multistage nature of MCM-41 formation,[7,9,12,14,30−34] a more detailed picture of silicate−surfactant interactions and how these trigger the formation of long-range order remains controversial. Some researchers have suggested that ionic silicates are strongly attracted to the surfaces of micelles and thereby promote sphere-to-rod transitions of silicate-coated micelles.[9,32,33,35] Regev[32] applied cryo-transmission electron microscopy (TEM) to study the intermediate structures formed before long-range ordering is obtained. They observed that addition of silicates promotes sphere-to-rod transitions of micelles, eventually yielding clusters of elongated micelles.[32] Lee et al.[33] and Albuquerque et al.[35] also observed sphere-to-rod transitions in aqueous cationic surfactant solutions when silicates were introduced into solution. A slight modification to this scenario of silica-coated micelles posits that

dx.doi.org/10.1021/la304475j | *Langmuir* 2013, 29, 766−780

disordered silica−micelle aggregates produce hexagonal long-range ordering through Ostwald ripening by internal reorganization.[34,36]

A substantially different picture has been put forth by Zana et al., who performed spectrofluorometry (pyrene emission spectra) and time-resolved fluorescence quenching measurements to study the effect of adding sodium silicate to CTAB and CTAC micellar solutions under MCM-41 synthesis conditions.[37,38] Their fluorescence data suggest that adding silicates has little impact on micelle aggregation number, prompting Zana et al. to conclude that silicates do not coat surfactant micelles in the early stages of MCM-41 formation. Instead, Zana et al. surmise that silicate−surfactant complexes begin with free surfactants binding small silicate oligomers. In this picture, the micelles act as reservoirs of free surfactant molecules, but it is otherwise unclear how long-range mesoscale order emerges.

The first scenario above (i.e., silica-coated micelles) suggests that silicate anions substantially displace bromide or chloride counterions surrounding micelles in the early stages of MCM-41 formation, while the second scenario (i.e., silicates interacting with free surfactants) refutes such substantial ion exchange. Several studies have been reported to address this issue. Galarneau et al. performed elemental analyses on CTAB/SiO_2/Na solids formed after 16 min and observed no detectable Br, prompting the conclusion that bromide/silicate ion exchange had completed during the first minutes of the synthesis. The pyrene fluorescence lifetime measurements carried out by Zana and co-workers[37,38] on CTAB systems report that only 16% of micelle-bound bromide ions are exchanged by OH^- and silicate ions. Vautier-Giongo and Pastore[39] carried out conductivity and pyrene fluorescence quenching measurement for less concentrated systems and observed that 30−40% of bromide ions are replaced by $Si(OH)_3O^-$. EPR experiments by Baute et al.[40] showed that silica-bound probes locate in the micelle−water interface region, suggesting that silicates interact preferentially with micelles and not with free surfactant monomers. Despite all this research, the question of halide/silicate ion exchange remains controversial. Our focus in the present work is to develop and apply a model of MCM-41 formation treating both surfactant self-assembly and silicate polymerization. In the base case of this model reported herein, we assume complete halide/silicate ion exchange consistent with the silica-coated micelles picture described above, and compare our results with experimental data on MCM-41 structure and formation. In a forthcoming publication, we will investigate the effect of halide/silicate ion exchange on the results obtained below.

Although it is generally accepted that silica networks in MCM-41 materials lack the crystalline order observed in, e.g., zeolites,[3,10] some structural insights have been gleaned from Raman and high-energy X-ray studies. The Raman spectra of MCM-41 reported by Chen et al.[8] were found to match stretching vibrations of 3-membered rings in amorphous oxides and glasses,[41] which are different from vibrations of such rings in crystalline silica.[42] More recently, Wakihara et al. reported high-energy X-ray studies comparing structural features in bulk amorphous silica to those in the mesoporous solids MCM-41 and SBA-15.[43] They found that the mesoporous silicas exhibit larger fractions of 3- and 4-membered rings and broader ring-size distributions compared to those of bulk amorphous silica (an n-membered ring is defined as a closed loop containing n tetrahedra linked by bridging oxygens $[-Si-O-]_n$). However, due to the amorphous nature of atomic connectivities in such mesoporous materials, it remains challenging for current experimental techniques to provide more detailed information about the atomic structures of silica mesopore walls. Instead, molecular simulations are poised to provide additional insights into mesopore structure and formation.

Simulating the formation of mesoporous silica materials remains challenging because of the simultaneous interplay among hydrophobic forces, electrostatic interactions, three-dimensional polymerization reactions, and phase equilibria. A comprehensive model that captures this broad range of effects is thus required to describe the formation process. On the other hand, large system sizes and long simulation times are also needed to observe the self-assembly of mesoporous materials, pointing to the seemingly incompatible need for simple, computationally tractable models. Because of this difficulty, only a few attempts at molecular modeling have been reported to address this problem.[25,26,44−50]

Schumacher et al. implemented kinetic Monte Carlo simulations to study the formation of periodic mesoporous silica.[48] Instead of simulating the self-assembly of surfactant molecules in the presence of silica, they studied silicate polymerization around preformed micelles represented as parallel cylindrical pipes. Their study produced plausible atomic structures of MCM-41 silica walls, which were used as the basis for nitrogen adsorption isotherm simulations. Reasonably good agreement with experiment was obtained. On the other hand, the model does not address the cooperativity between silica and the surfactant in determining the mesoscale structure.

Jorge et al. carried out molecular dynamics simulations using more detailed models to investigate the early stages of silica mesopore synthesis.[49,50] They observed that anionic silicates interact very strongly with cationic surfactants, adsorbing significantly on the surface of micelles and displacing some of the previously bound bromide counterions; this finding provides additional support for the notion of silica-coated micelles. Despite this progress, their simulations suffered from length and time scale limitations and therefore were unable to describe later stages of MCM-41 formation. Given current computer capabilities, some extent of coarse-graining is thus needed to address these issues.

Lattice models can be viewed as discretizations of three-dimensional space onto fixed arrays of sites. Such discrete models have been applied to study silica nanoparticles,[51−53] crystalline microporous zeolite analogues,[54] and surfactant-templated mesoporous silica.[25,26,44−47] Siperstein and Gubbins performed lattice model simulations to study the phases of surfactant−inorganic−solvent ternary systems,[25,26] finding hexagonal and lamellar mesostructures whose appearance is controlled by the surfactant-to-silica ratio, in agreement with experiments. Their model was later extended to study the formation of hybrid organic−inorganic materials.[44−47] However, this model lacks the effect of silica condensation, which is the second main step in MCM-41 formation. Recently, we developed an atomic lattice model of silica polymerization that captures the behavior of both amorphous[55] and crystalline forms of silica.[54] Below, we apply this model to the ternary surfactant−silica−solvent system to examine the two-step synthesis procedure, finding reversible lamellar/hexagonal phase changes, the formation of MCM-41 after long simulations, and new information on the nature of amorphous silica in MCM-41.

The remainder of this article is organized as follows: in section II, we describe the lattice model and its parameters; in section III, we detail the various Monte Carlo simulation methods; in section IV, we give the results and discussion of the simulated two-step MCM-41 synthesis including structural analysis; and in section V, we offer a summary and concluding remarks.

MODEL DESCRIPTION

Lattice Model Representation. We focus on alkaline solution synthesis of siliceous mesoporous materials starting with aqueous silica sources (no alumina) and surfactant molecules. We combine our model of silica polymerization[54,55] with the model of Larson for surfactant−water systems, and this builds on the earlier work of Siperstein, Gubbins, and co-workers.[25,26] One commonly used silica source is tetraethyl-orthosilicate (TEOS), which undergoes complete hydrolysis at high pH and water-to-silica ratios to yield ethanol and silicic acid, $Si(OH)_4$. We consider alkyl-trimethyl ammonium bromide (ATA-Br) as the surfactant and sodium hydroxide (NaOH) as the base, yielding a solution with the following ionic species: ATA^+, Br^-, Na^+, and OH^- in addition to various anionic silica species. Such an MCM-41 synthesis thus involves water/ethanol solutions containing $Si(OH)_4$, ATA^+, Br^-, Na^+, and OH^-. We seek a simplified representation of this system, containing the essential ingredients for MCM-41 formation. We begin by treating water and ethanol as identical solvent molecules, denoted by "S", and represented as lattice vacancies. We explicitly represent $Si(OH)_4$ and ATA^+ species in our lattice model simulations, as detailed below. We do not explicitly represent Br^-, Na^+, or OH^-; however, the precise number of OH^- present in our system, which reflects the solution pH, is a key variable that we track for use in the Monte Carlo probabilities described below. Due to computational cost, we ignore the ion exchange between bromide and silicate anions, and assume that surfactant cations interact directly with silicate anions, as explained below. We are aware of anionic effects on the formation of mesoporous solids, as anions not only affect the rate of silicate hydrolysis but also play an important role on the morphology, order, and porosity of the final products.[56] In this study, we endeavor to keep our model as simple as possible while retaining practical representations of the real synthesis.

Our lattice model is based on a body-centered cubic (bcc) lattice, which can be viewed alternatively as[57] (i) two interpenetrating diamond lattices thus facilitating a tetrahedral representation of $Si(OH)_4$ species as we have done in our earlier work[54,55] or (ii) two interpenetrating simple-cubic (sc) lattices. In what follows, we represent each surfactant molecule as occupying several connected sites on one sc sublattice[58−60] of the overall bcc lattice and each $Si(OH)_4$ species as occupying several connected sites on a diamond sublattice of the same, overall bcc lattice. By using the simple cubic lattice for the surfactant, we were able to test our model against the previous work on surfactant water systems.[25,26,61,62]

Surfactant Molecules. These are represented as H_iT_j, with i hydrophilic head groups (H) and j hydrophobic tail groups (T) occupying chains of connected sc lattice sites. This model of amphiphilic assembly was originally proposed by Larson;[58−60] we follow Larson's specification that lattice sites within one cube-diagonal distance ($\sqrt{3}$ times the base sc lattice distance) are defined as connected sites with an equal magnitude of interaction. For example, the interactions between the site (0, 0, 0) and sites at (0, 0, 1), (0, 1, 1,), and (1, 1, 1) are taken to be the same, although their distances differ. The coordination number of Larson's surfactant model is 26, including 6 nearest neighbors, 12 face-diagonal neighbors, and 8 cube-diagonal neighbors. For direct comparison with Larson's previous results,[58−60] we allow occupation of surfactants on only one sc sublattice of the overall bcc lattice. We focus herein on H_4T_4 surfactants, which model the limit of short alkyl chains in alkyl-trimethyl ammonium species.

Silicic Acid Si(OH)$_4$. Our atomic lattice model of silicic acid polymerization has been described in detail elsewhere;[55] here we briefly summarize the model. We represent $Si(OH)_4$ molecules as rigid tetrahedra on the bcc lattice by coarse graining OH groups into single particles. We thus assume that Si atoms, OH groups, and H_2O molecules occupy the same effective volume. As such, each $Si(OH)_4$ tetrahedron occupies five bcc sites. Each $Si(OH)_4$ unit moves on the lattice via translation and rotation. Because the bcc lattice is equivalent to two interpenetrating diamond sublattices, the reorientation move corresponds to switching tetrahedral vertices from one diamond sublattice to the other.

We represent silica condensation, the conversion of terminal OH groups to bridging oxygens by the process ≡Si—OH + HO—Si≡ ⇌ ≡Si—O—Si≡ + HOH, by a process where the OH groups from two tetrahedral vertices come together at a given site to create a bridging oxygen and a water molecule which occupies the site vacated by one of the tetrahedral vertices.[55] This approach allows the sampling of silica condensation/hydrolysis reactions while maintaining intact tetrahedra throughout.

In alkaline aqueous solutions, the distribution of silicate species is governed by deprotonation equilibria, with the first two deprotonation equilibrium constants for silicic acid given by

$$K_1 = \frac{[Si(OH)_3O^-][H^+]}{[Si(OH)_4]} \quad (1)$$

$$K_2 = \frac{[Si(OH)_2O_2{}^{2-}][H^+]}{[Si(OH)_3O^-]} \quad (2)$$

where pK_1 and pK_2 at STP are 9.5 and 12.6, respectively.[63] The doubly deprotonated molecules $Si(OH)_2O_2{}^{2-}$ do form at high enough pH; however, they are relatively unreactive in polymerization reactions.[64] At pH 11 and an ionic strength of 1 M, the mole fraction of $Si(OH)_2O_2{}^{2-}$ is less than 5%, and when the pH drops below 10.5, the $Si(OH)_2O_2{}^{2-}$ species essentially vanishes.[63] As such, to avoid unnecessary complexity in our model, we consider only singly deprotonated $Si(OH)_3O^-$ molecules, henceforth called ionic silica and denoted as "S_I". One oxygen in each tetrahedron representing S_I is chosen at random and marked as negatively charged in our lattice model. Such anionic oxygens do not participate in polymerization in this model, and as such are precluded from engaging in condensation reaction with OH groups or other O^- anions. In contrast, the three OH groups on S_I and all four OH groups on neutral silicic acid (denoted as "S_N") can engage in polymerization.

With these definitions, the molecular species in our lattice model are as follows: one solvent S in each vacant site; surfactant H_4T_4 occupying eight connected simple-cubic sites; neutral and anionic silica monomers, S_N and S_I, respectively, each occupying five tetrahedrally arranged sites on the bcc

dx.doi.org/10.1021/la304475j | Langmuir 2013, 29, 766−780

lattice. We find it most convenient to specify the lattice model interactions among the following five species: H, T, S, S_N, and S_I. Only two-body interactions are considered; the interaction energy between pairs is labeled by ε_{ij} (i, j = H, T, S, S_N, S_I). We begin by describing the physical, intermolecular interactions between surfactant and silica species; we then detail the chemical, polymerization energies between S_N and S_I species.

Under conditions where silica condensation can be neglected, the total energy of the system is given by

$$H = \frac{1}{2}\sum_i \sum_j N_{ij}\varepsilon_{ij} \tag{3}$$

where N_{ij} is the total number of neighbors with interaction energy ε_{ij} within a certain cutoff distance, chosen from prebuilt neighbor lists between components i and j. As discussed previously by Siperstein and Gubbins,[26] Monte Carlo simulations of the surfactant−water system on the SC lattice require only the net energy change between two configurations (this does not apply to the interactions involving silica species in our model). This energy change depends only on the interchange energy of replacing species i with species j, given by $\omega_{ij} = \varepsilon_{ij} - {}^1/_2(\varepsilon_{ii} + \varepsilon_{jj})$. In what follows, the reduced temperature is defined as $T^* = k_BT/|\omega_{HT}|$, where k_B is Boltzmann's constant and ω_{HT} is the head−tail interchange energy. All other interaction energies are also defined relative to $|\omega_{HT}|$. The surfactant−solvent interchange energies used in our model satisfy $\omega_{HT} = \omega_{ST}$ and $\omega_{HS} = 0$, following Panagiotopoulos and co-workers.[62,65,66] This reflects the fact that polar head groups (H) and dipolar solvent species (S) are generally hydrophilic, and hence are interchangeable and share similar interchange properties with tail groups (T).

It is known that the solubility of silica increases dramatically with solution pH,[63] and also depends on alcohol content.[67] In this paper, we only consider the case where silica and solvent are completely miscible ($\varepsilon_{S-SI} = 0 = \varepsilon_{S-SN}$). Other situations where inorganic species are either partially miscible or completely immiscible will be discussed in future work.

We impose strong attractions between silica and surfactant head groups with $\varepsilon_{H-SI} = \varepsilon_{H-SN} = -2$, which are justified as follows. For ionic silica, the major contributor to ε_{H-SI} is the electrostatic attraction between anionic silica and cationic surfactant head groups. Therefore, a given H−S_I attraction in our model depends on the position of the negatively charged oxygen in S_I. The H−S_N attraction is dominated by several charge−dipole interactions between the charge in H and the OH local dipoles in S_N.[68] For simplicity, we adopted the same strength for H−S_I and H−S_N attractions in the present model. The strong affinity between silicate and surfactant provides the driving force for mixing of these components, and for phase separation of silicate/surfactant from the solvent-rich phase, as found by other researchers who used this same parameter set.[26,45]

Regarding interaction length scales, the H−S_N attraction takes effect when the distance between a surfactant headgroup and a central silicon atom of an S_N group is within $\sqrt{3}$ of the base bcc lattice distance. In contrast, an H−S_I attraction takes effect when a negatively charged oxygen and a surfactant headgroup are within this same $\sqrt{3}$ lattice distance. Given the current representation of our bcc lattice model, the $\sqrt{3}$ lattice distance includes 58 neighboring sites and corresponds to a distance of 3.2 Å, which is twice the typical Si−O bond length. The interaction parameters ε_{ij} relative to $|\omega_{HT}|$ are given in Table 1.

Table 1. Interaction Parameters (ε_{ij})

ε_{ij}	H	T	S	S_I	S_N
H	0	0	0	−2	−2
T	0	−2	0	0	0
S	0	0	0	0	0
S_I	−2	0	0	0	0
S_N	−2	0	0	0	0

Now considering silica polymerization, we assume for simplicity that formation of bridging oxygen in S_N−S_N and S_N−S_I condensations carry the same stabilization, denoted by the generic silica condensation energy $\varepsilon < 0$. Below, we discuss this energy in comparison with the head−tail interchange energy scale $|\omega_{HT}|$. In our previous work on silica polymerization,[55] we found that applying small penalties on 3- and 4-membered rings, which arise very naturally in the present lattice model, is necessary to produce a realistic model of amorphous silica. As in our previous work, the penalties on each 3- and 4-ring were taken to be $\varepsilon_3 = 0.6|\varepsilon|$ and $\varepsilon_4 = 0.3|\varepsilon|$, respectively.

Model Parameterization. In our previous work on this bcc lattice model, we found that the silica condensation energy of $\varepsilon = -4.0$ kcal/mol = −16.7 kJ/mol was found to reproduce silica solubility in water at low pH and STP.[55] The challenge is thus to relate this energy scale to the $|\omega_{HT}|$ interchange energy. To construct this connection, we simulated the H_4T_4−solvent binary system over a range of H_4T_4 volume fractions. At certain volume fractions, we carried out canonical ensemble simulations at various temperatures and recorded the highest temperature at which ordered phases (i.e., hexagonal or lamellar) formed.

The simulated H_4T_4−solvent phase diagram is plotted in Figure 1a, whereas Figure 1b shows a schematic phase diagram of C_{16}TMABr in water based on experimental data from Brinker et al.[24] Although there are quantitative differences between the experimental and simulated phase diagrams (Figure 1), they show qualitative agreement, especially at higher surfactant concentrations in the hexagonal and lamellar regimes. The interchange energy $|\omega_{HT}|$ was calibrated by comparing the highest simulated and experimental temperatures that form the hexagonal phase. The resulting order−disorder transition temperatures are $T^*_{MC} = 8.6$ for simulation and $T_{exp} = 508$ K from experiments, suggesting the value $|\omega_{HT}| = k_B \times (508\ \text{K})/8.6 \approx 0.5$ kJ/mol or $|\omega_{HT}|/k_B = 59$ K. We thus arrive at the relation between the fundamental energy scales in our model: $|\varepsilon/\omega_{HT}| \approx 30$, indicating that silica condensation energetics are more than an order of magnitude larger than surfactant−surfactant and surfactant−silica attractions.

SIMULATION METHODOLOGY

To study MCM-41 formation and structure, we have employed a variety of molecular simulation techniques as detailed below. Most of the results were obtained from canonical ensemble Monte Carlo simulations. We also implemented reactive ensemble MC (REMC) to treat the deprotonation equilibrium of silicic acid. All Monte Carlo simulations were carried out with periodic boundary conditions in three dimensions.

Canonical Ensemble Simulation. To sample surfactant molecule configurations, we implemented MC moves involving chain reptation, chain twisting,[58] cluster moves, and chain

dx.doi.org/10.1021/la304475j | Langmuir 2013, 29, 766−780

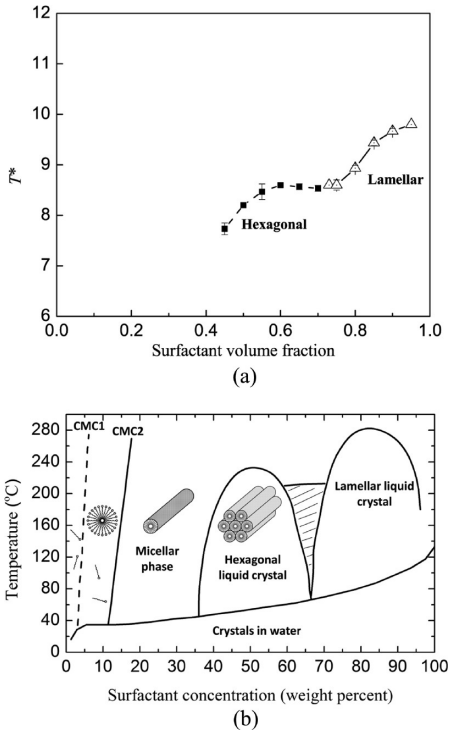

Figure 1. Phase diagram for the surfactant−solvent system. (a) Simulated phase diagram for the H_4T_4−solvent system. Symbols are results from canonical ensemble simulations averaged over three statistically independent runs, and error bars show one standard deviation. Black squares and open triangles represent hexagonal and lamellar phases, respectively. Lines are plotted to guide the eyes. (b) Schematic phase diagram for C_{16}TMABr in water, data taken from Brinker et al.[24]

regrowth (partial and complete regrowth) using configurational-bias Monte Carlo.[69−71] Various mixes of MC moves were chosen on the basis of the components and compositions of the system. For binary surfactant−solvent systems at low surfactant concentrations (micellar regime of the phase diagram), the typical mix of MC moves was 50% complete regrowth, 49.9% reptation, and 0.1% cluster moves. Two surfactant molecules were considered part of the same cluster if they are connected by at least one tail−tail attraction. Our cluster moves followed the spirit of the Swendsen−Wang algorithm.[72] In particular, an entire cluster was shifted by one first-neighbor distance (i.e., the shortest possible displacement on the bcc lattice) in random directions, hence obeying detailed balance.[73] If clusters move in such a way that a new, larger cluster forms by the aggregation of the individual clusters, the cluster move was rejected because of the violation of microscopic reversibility, since in the next step these clusters would be considered as a single cluster.[73]

We tested our simulation approach for the binary system (H_4T_4−solvent) by comparing the volume fraction of micelles at different temperatures (T^* = 6.5 and 8.0) and compositions with the simulation studies of Floriano et al.[62] Our volume fractions showed excellent agreement with the grand canonical ensemble results of Floriano et al.

For the ternary system containing solvent, surfactant H_4T_4 species, and also silica (neutral S_N and/or anionic S_I species), both rotational and translational moves of silica tetrahedra were implemented. The rotational move corresponds to switching tetrahedral vertices from one diamond sublattice to the other. The translational move was attempted by moving a silica tetrahedron to any location in the simulation box while keeping its orientation unchanged, i.e., by fixing its sublattice and the relative position of the negatively charged oxygen if moving an S_I. Other than chain regrowth moves which were accepted or rejected on the basis of the configurational-bias Monte Carlo scheme, the remainder of MC moves were accepted according to the standard Metropolis criterion determined by the Boltzmann factor associated with the configurational change.[71]

Reaction Ensemble Monte Carlo. As discussed above, the composition of silica solutions depends strongly on pH.[20,63,74] We treat the influence of pH in our simulations using reactive ensemble Monte Carlo[27,28] (REMC) to model silicic acid deprotonation equilibria. In our simulations, we consider the singly ionized silicate anion $S_I = Si(OH)_3O^-$ generated through the following reaction:

$$\equiv Si{-}OH + OH^- \rightleftharpoons \equiv Si{-}O^- + H_2O \tag{4}$$

The equilibrium coefficient for eq 4 depends on local silica structure through its Q_n value, i.e., the number of bridging oxygens surrounding a given Si center. Using the definitions of the aqueous acid equilibrium constant, $K_a \equiv [H^+][A^-]/[HA]$, and that of $K_w \equiv [H^+][OH^-]$, we use the following formula for K_D:

$$K_D(n) = \frac{K_a^1(n)[H_2O]}{K_w} \tag{5}$$

where $K_a^1(n)$ are the first acid ionization coefficients for Q_n silica species. We assume the molarity of water to be 55.6 mol/L, a pK_w value of 14, and we use the $pK_a^1(n)$ values shown in Table 2 from White et al.[75] The resulting values of $K_D(n)$ are shown in Table 2.

Table 2. Equilibrium Constants for Silicate Speciation

species	Q_0	Q_1	Q_2	Q_3
pK_a^1	9.5[63]	9.85[63]	11.2[76]	11.2[76]
K_D	1.76×10^6	7.9×10^5	3.5×10^4	3.5×10^4

The REMC scheme we have used for sampling silica acid/base reactions is given in flowchart form in Figure 2. The process begins by randomly choosing one silica tetrahedron. If an S_N molecule is selected, the forward reaction in eq 4 is attempted by replacing the S_N with an S_I, keeping the same sublattice orientation but with random location of the newly formed O^-, and by updating the numbers of OH^- and H_2O. We note that, although OH^- is not explicitly represented in our lattice model, we keep track of the total number of OH^- groups in the system for computing REMC probabilities as described below. If an S_I is selected, we attempt the reverse of eq 4. Focusing now on the forward reaction, we next identify n = the number of bridging oxygens around the chosen S_N; if $n = 4$, the deprotonation move is aborted for lack of protons, while, if $n \leq 3$, the appropriate value of $K_D(n)$ from Table 2 is extracted. The energy change ΔE from replacing S_N with S_I is then calculated for use in the following REMC probability:[51]

$$p = \min\left\{1, \exp(-\Delta E/k_BT)K_D(n)\frac{N_{S_N}N_{OH^-}}{(N_{S_I}+1)(N_{H_2O}+1)}\right\} \tag{6}$$

If the forward reaction MC move is accepted, the numbers N_{SI} and $N_{solvent}$ increase by 1, while N_{SN} and N_{OH^-} decrease by 1

dx.doi.org/10.1021/la304475j | Langmuir 2013, 29, 766−780

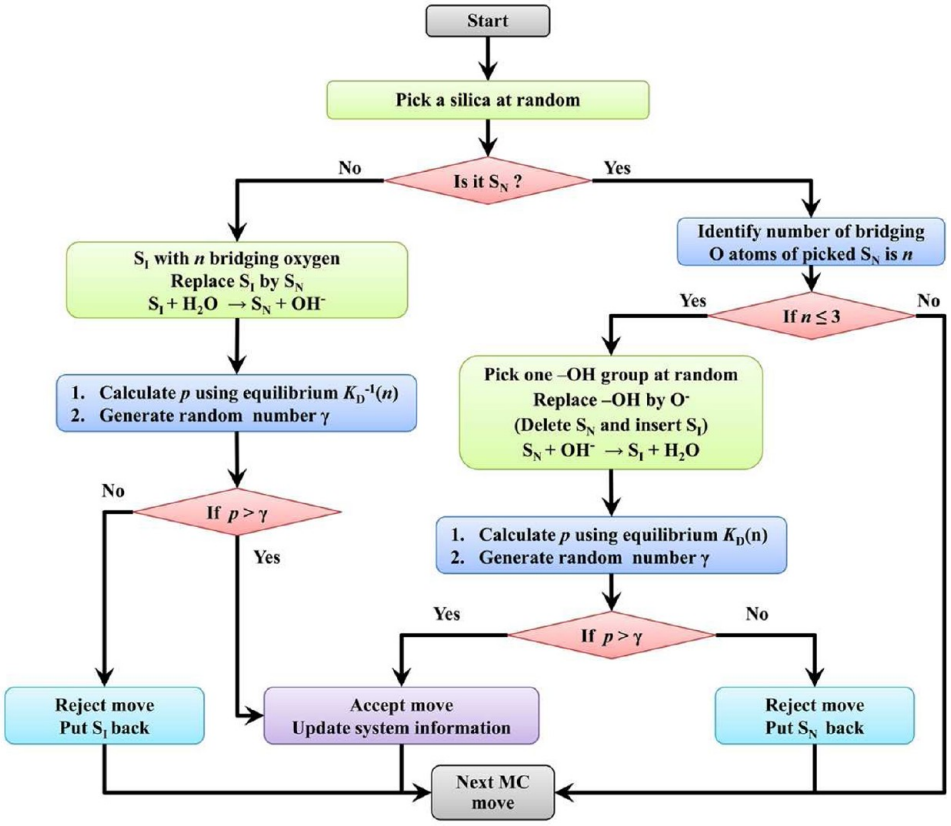

Figure 2. Flowchart of the steps involved in silica acid/base Monte Carlo moves.

(and vice versa for the backward reaction). The backward reactive move is accepted with the probability

$$p = \min\left\{1,\ \exp(-\Delta E/k_B T)\frac{1}{K_D(n)}\frac{N_{S_I}N_{H_2O}}{(N_{S_N}+1)(N_{OH^-}+1)}\right\} \quad (7)$$

We note that, although S_N and S_I share the same interaction parameters in Table 1, these interactions are computed from different reference points in the lattice (Si atom in S_N and O^- atom in S_I). As such, S_N/S_I replacements can change the system energy. We also note that, although N_{SN} and N_{SI} fluctuate during REMC, the total number of tetrahedra = $N_{SN} + N_{SI}$ is conserved during REMC.

Two-Step Synthesis. As discussed above, MCM-41 syntheses typically proceed via two steps: the first at low temperature and high pH where silica condensation can be neglected and the second at higher temperature and sometimes lower pH where silica condensation becomes relatively rapid. We modeled this two-step approach by defining an initial stage of the MC simulation in which the silica condensation energetics were set to zero, i.e., $\varepsilon = \varepsilon_3 = \varepsilon_4 = 0$. Although double occupancy of OH groups is allowed during this stage, there is no thermodynamic driving force to maintain connections between neighboring tetrahedra. As a further simplification, we note that, at pH 11, approximately 95% of silicic acid is deprotonated in the form of ionic silica.[63] As such, the first stage of the simulation starts with all ionic silica S_I, and no REMC moves between S_I and S_N were considered during this stage. The real silica–surfactant system contains a mixture of monomers, dimers, cyclic trimers, cyclic tetramers, double three-rings (D3R), and other silica oligomers,[14] as is found in silica polymerization systems as short times even when the monomers are the dominant species.[77] The distribution of silicate species is greatly affected by the synthesis conditions such as pH, cosolvent, temperature, and other factors. In the study of Firouzi et al.,[14] the aqueous-rich phase contained 47–80% monomers, whereas the silicate–surfactant-rich phase was dominated by double four-rings (D4R) due to the addition of a D4R-stabilizing agent to suppress silicate condensation. In future work, we will study the effect of silica oligomers on the formation of MCM-41 materials.

After silicate–surfactant liquid crystal mesostructures formed exhibiting long-range order, we initiated the second stage of the simulation with REMC sampling of acid–base equilibria, and silica condensation controlled by the following energy parameters: the silica condensation energy $\varepsilon = -30|\omega_{HT}|$, the three-ring penalty $\varepsilon_3 = +18.0|\omega_{HT}|$, and the four-ring penalty $\varepsilon_4 = +9.0|\omega_{HT}|$ as discussed above. Initial conditions for N_{OH^-} were determined by system pH. A pH of 10 corresponds to $N_{OH^-} = 0.72$ in the 30 × 30 × 240 lattice; this rounds up to $N_{OH^-} = 1$ initially. We also considered a pH of 11 which gives $N_{OH^-} = 7$ initially and a pH of 12 which gives $N_{OH^-} = 72$ initially. In all cases, the value of N_{OH^-} was reset to its initial value after 1000 MC steps to simulate a buffering effect of keeping pH constant.

Simulation Details. Ternary surfactant–silica–solvent systems were studied using the "direct interfacial method" following Panagiotopoulos and co-workers, where one dimension (z) of the simulation box was 8 times the size of the other two directions.[65] The elongated z dimension favors the formation of planar interfaces which helps to interpret the

dx.doi.org/10.1021/la304475j | Langmuir 2013, 29, 766–780

properties of the surfactant−silica-rich phase. The box size used in simulations was 30 × 30 × 240 bcc sites on each edge.

In this study, we start with 100% silica monomers randomly distributed in the system. Two silicic acid molecules were considered part of the same cluster if they share one bridging oxygen atom. Cluster sizes of surfactant and/or silica phases were calculated using the Hoshen−Kopelman cluster-counting algorithm.[78] Ring-size distributions were calculated using the algorithm proposed by Yuan et al.[79] where only fundamental rings (defined as rings that cannot be divided into two smaller rings) were counted.

In what follows, we define one MC "step" as attempts to move each of the N_{chain} H_4T_4 surfactants, and each of the N_{SN} + N_{SI} silica tetrahedra, once. A typical mix of MC moves during stage 1 included 20% complete chain regrowth, 20% partial chain regrowth, 58% chain reptation, 1% silica tetrahedron translation, and 1% silica rotation. In contrast, during stage 2, the MC moves involved 20% complete chain regrowth, 20% partial chain regrowth, 58% chain reptation, 0.02% silica acid/base reactions, 0.99% silica translation, and 0.99% silica rotation.

The concentrations of species c_i were defined as the total number of a certain kind of molecule divided by the total number of bcc sites $(N_{site}) = 2 \times L_x \times L_y \times L_z$, where L_x, L_y, and L_z are the numbers of bcc lattice sites in the simulation box along x, y, and z directions, respectively. A typical example of concentrations studied during stage 1 involves $c_{H_4T_4} = 0.009\,375$ and $c_{S_I} = 0.015$. The former value represents 15% of the maximum possible surfactant concentration (1/16); the latter is 24% of the concentration of β-cristobalite (0.0625), which is the densest form of silica we have sampled in our bcc lattice model.[54] In a simulation box of 30 × 30 × 240, there are 6480 silica tetrahedra, 4050 surfactant H_4T_4 molecules, and 367 200 solvent molecules. For such a system, the typical CPU times for one MC step at stages 1 and 2 are 0.39 and 0.34 s on a 800 MHz AMD Opteron 6172 Processor.

RESULTS AND DISCUSSION

Phase Separation Induced by Adding Silica to Surfactant−Water System. We began by performing stage 1 simulations, i.e., without silica condensation, studying the effect of surfactant−silica adhesion at relatively low concentrations of silica and surfactant. Spherical surfactant micelles were observed in our simulations, as seen in Figure 3a for c_{S_I} = 0, $c_{H_4T_4} = 0.009\,375$, and $T^* = 6.5$. Parts b and c of Figure 3 show the effect of increasing silica concentration to $c_{S_I} = 0.005$ and 0.015, respectively, while keeping the surfactant concentration fixed at $c_{H_4T_4} = 0.009\,375$, and temperature at $T^* = 6.5$. Figure 3b and e shows a core−shell structure involving surfactant−micelle cores partially coated with anionic silica tetrahedra. This core−shell arrangement represents the inverse of that seen in silica−template nanoparticles that act as precursors in the formation of the zeolite silicalite.[51,53] The inverted core−shell structure seen in Figure 3b likely results from the relative concentrations of silica and surfactant, and from our neglect of silica condensation in the present stage 1 simulations.

When increasing the silica concentration to $c_{S_I} = 0.015$, the system undergoes a phase change, as shown in Figure 3c, involving a surfactant−silica-rich phase in equilibrium with a solvent-rich phase. The surfactant−silica phase was found to exhibit a hexagonal array of cylindrical pores, i.e., the signature mesostructure of MCM-41. We note that, in the absence of silica, this system resides in the micellar region of the surfactant−solvent phase diagram (Figure 3a). As such, the MCM-41-like mesostructure found in our simulations arises as a collective property of surfactant and silica, in agreement with the cooperative templating hypothesis.

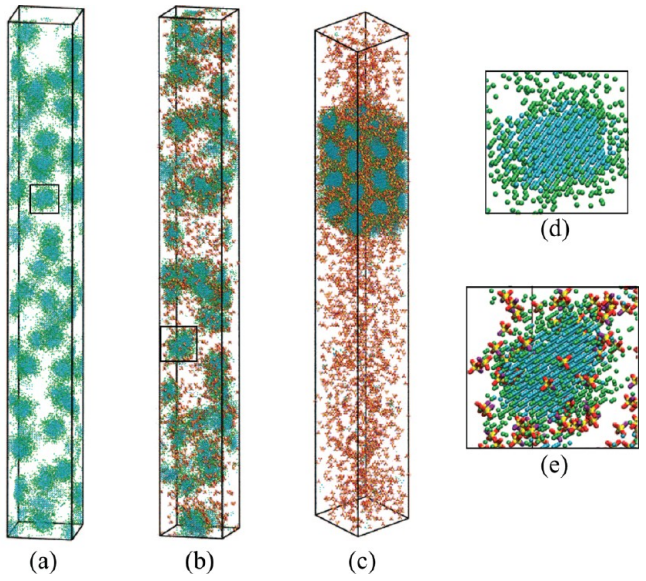

Figure 3. Phase separation when silica is added to the H_4T_4−solvent system at $T^* = 6.5$, for a system size of 30 × 30 × 240. (a) Roughly spherical micelles formed in binary surfactant−solvent system at $c_{H_4T_4} = 0.009375$. (b) Ternary surfactant−silica−solvent system with the same H_4T_4 concentration but with $c_{S_I} = 0.005$. (c) Same as (b) but with $c_{S_I} = 0.015$. (d) and (e) show two amplified views (×5) of systems focusing on a single micelle in snapshots of (a) and (b), respectively. Blue and green spheres represent tail and head groups of surfactant molecules, respectively, whereas red and purple spheres illustrate neutral and negatively charged oxygens, and yellow spheres at the centers of silica tetrahedra show silicon atoms.

We carried out a structural analysis of micelles when increasing silica concentration from zero to 0.005. Because Chen et al. reported the formation of rod-like micelles upon addition of silica,[9] we investigate how the shapes of our simulated micelles change with silica concentration. To do this, we define an aspect parameter $\eta = r_{max}/r_{min}$ to describe the structure of particles. As shown in Figure 4a, r_{min} is defined as the largest radius of a sphere that is 30% full of particles. The value of 30% was chosen to visually match the contour of spherical particles. r_{max} is defined as the smallest radius of a sphere that contains 95% of a given coated micelle. In principle, an aspect ratio parameter of unity indicates roughly spherical micelles, while a value significantly greater than 1 suggests elongated micelles.

We plot the aspect ratio parameter η versus micelle index in Figure 4b when silica is added to the H_4T_4−solvent system at $T^* = 6.5$. The addition of silica leads to larger and fewer micelles: there are 46, 39, and 29 micelles at silica concentrations c_{S_I} = 0, 0.025, and 0.005, respectively. When no silica is present in solution, almost all micelles exhibit η values near unity, indicating spherical micelles in the binary H_4T_4−solvent system. When the silica concentration is increased to $c_{S_I} = 0.005$, several micelles evolve to elongated

dx.doi.org/10.1021/la304475j | Langmuir 2013, 29, 766−780

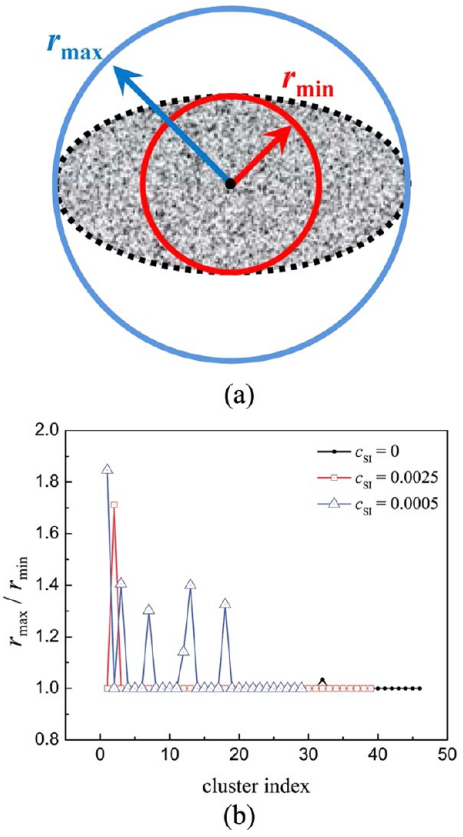

Figure 4. Aspect ratio analysis of micelles when silica is added to the H_4T_4–solvent system at T^* = 6.5, for a system size of 30 × 30 × 240, $c_{H_4T_4}$ = 0.009 375. (a) Two-dimensional definition of r_{min} and r_{max} for an elliptical particle. The shaded area represents the morphology of an elliptical micelle. (b) Aspect ratio for micelles at silica concentrations c_{S_i} = 0, 0.0025, and 0.005, showing more elliptical micelles as silica concentration is increased.

ones, as shown by open blue triangles in Figure 4b. This result, which agrees with the interpretation of ^{14}N NMR data reported by Chen et al.,[9] presumably occurs because silica–surfactant attractions drive the micelles to increase their surface areas, hence distorting away from spherical shapes.

Reversible Transformation between Lamellar and Hexagonal Phases. As discussed in the Introduction, the surfactant–silica mesophase has been found experimentally to exhibit lyotropic liquid-crystalline behavior during stage 1 of the synthesis, i.e., before the onset of silica condensation. In particular, Firouzi et al.[14] observed a reversible lamellar-to-hexagonal phase transition of the surfactant–silica mesophase when heating/cooling between 25 and 60 °C, suggesting that the final mesophase is controlled by thermodynamic equilibrium in stage 1. We modeled this phenomenon through stage 1 simulations (i.e., simulations without silica polymerization) of the surfactant–silica mesophase by decreasing the temperature to T^* = 5.5 and then reheating back up to T^* = 6.5 (this reduced temperature range corresponds to about 51–110 °C). As shown in Figure 5c and d, we have found reversible transformations between hexagonal and lamellar mesophases, in agreement with the experiments of Firouzi et al.[14] The simulated phase change from heating lamellar (T^* = 5.5) to hexagonal (T^* = 6.5) required many fewer MC steps than the reverse cooling transition, also in qualitative agreement with experiment. However, our use of complete surfactant regrowth with random replacement anywhere in the simulation cell (i.e., Glauber dynamics) ignores diffusion limitations, and hence precludes quantitative comparisons with experimental relaxation times.

Also shown in Figure 5 are results of stage 2 simulations, which include silica acid/base and polymerization reactions. We describe these more fully in the next section; here, we briefly discuss these stage 2 simulations as they pertain to the lamellar-to-hexagonal phase transition. Figure 5b and c shows the effect of silica condensation on the lamellar phase. Although the

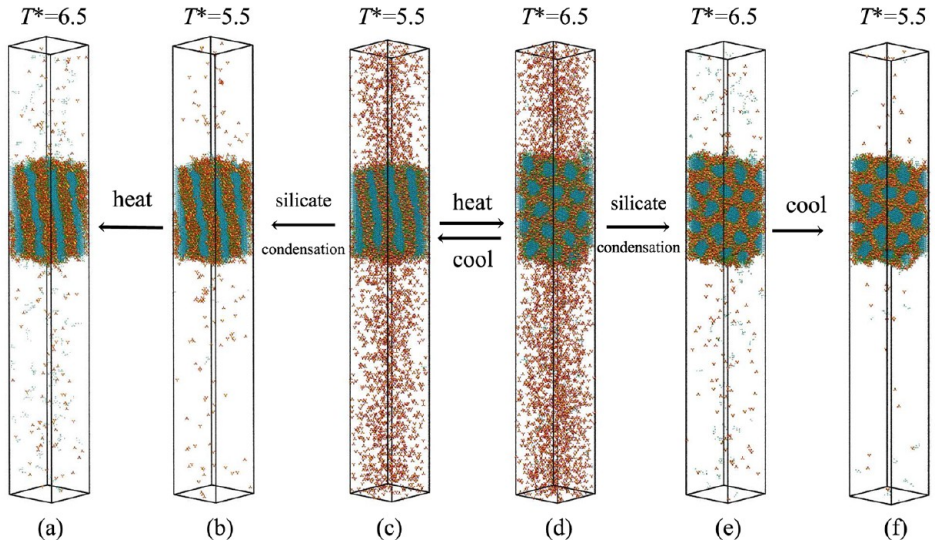

Figure 5. Reversible lamellar–hexagonal phase transition, simulated with canonical MC with concentrations $c_{H_4T_4}$ = 0.009375 and c_{S_i} = 0.015 for a 30 × 30 × 240 system size. (c) Stage 1 simulation (no silica condensation) at T^* = 5.5 resulting in lamellar mesophase. (d) Stage 1 simulation at T^* = 6.5 resulting in hexagonal mesophase; cooling/heating between T^* = 5.5 and T^* = 6.5 produced reversible lamellar–hexagonal phase transitions in the stage 1 simulations. (b) Stage 2 simulation (with silica condensation) beginning with final configuration in (c). (a) Heating condensed lamellae to T^* = 6.5 showed no change in mesophase. (e) Stage 2 simulation beginning with the final configuration in (d). (f) Cooling condensed hexagonal phase to T^* = 5.5 showed no change in mesophase.

dx.doi.org/10.1021/la304475j | *Langmuir* 2013, 29, 766–780

overall mesostructure is largely unchanged, most of the silica tetrahedra become sequestered into the surfactant−silica-rich region of the simulation cell. Heating the lamellar phase from T^* = 5.5 to 6.5 (Figure 5a), which produced the hexagonal phase in stage 1 simulations, in this case gives no phase change because the silica condensation has "locked in" the lamellar mesostructure. Such behavior presumably arises from the substantial silica condensation energy, $|\varepsilon| = 30|\omega_{HT}|$, which produces a large free-energy barrier that precludes the system from reaching the thermodynamically stable hexagonal phase.

The story is much the same for stage 2 simulations of the hexagonal phase (Figure 5e and f). Sampling silica condensation pulls most of the silica into the hexagonal mesophase, which changes very little upon cooling from T^* = 6.5 to 5.5.

Effects of Silica Condensation. We now focus on the effects of silica condensation during stage 2 of our MC simulations. To investigate silica condensation, we have performed MC simulations at T^* = 6.5 (hexagonal phase region) on a 30 × 30 × 240 box with the following concentrations: $c_{H_4T_4}$ = 0.009 375 and c_{Silica} = 0.015. (We note that $c_{Silica} = c_{SN} + c_{S_l}$, which is constant though the individual concentrations fluctuate.) Above we found in Figure 5b and e that silica condensation concentrates most of the available silica into the surfactant−silica-rich mesophase. To quantify this effect, we plot composition profiles along the elongated z-axis in Figure 6a without (stage 1) and Figure 6b with (stage 2) silica condensation, using each plane of sites in the bcc lattice as a bin for compiling concentration statistics along the z-axis.

Figure 6a shows an accumulation during stage 1 of the simulation of both silica and surfactant concentration between lattice planes in the range z = 45−95. This dense region was observed to undergo a small amount of drift along the z-axis. In this dense region of the simulation cell, most of the surfactant and about half of the silica has concentrated to form the hexagonal mesophase discussed above. The local silica concentration at this stage is about 0.043, i.e., nearly 70% of the concentration of β-cristobalite on this bcc lattice. The local concentration profiles after silica condensation are given in Figure 6b, showing that essentially all the silica and surfactant have been pulled into the dense region at stage 2. The local silica concentration approximately doubles to about 0.085, i.e., 140% of the β-cristobalite concentration.

System snapshots corresponding to the composition profiles in Figure 6 are given in Figure 7. In particular, Figure 7a shows the initial condition of the MC simulation with surfactant and silicate molecules distributed randomly throughout the simulation cell. Figure 7b shows the result of the stage 1 simulation with the hexagonal mesophase located in the slab with z values in [45, 95], where z is the elongated dimension of simulation box with values between 1 and 240. Figure 7c shows the result of silica condensation during stage 2 pulling most of the silica and surfactant molecules into the mesophase. Figure 7d is the same as Figure 7c except that the surfactant molecules have been deleted from the image, showing the meso*porous* MCM-41 that would result in an experimental synthesis from calcination.

All the modeling results reported thus far have come from the simulated two-stage synthesis approach discussed above, wherein fluid mesostructures with long-range order arise in stage 1, followed by silica acid/base reactions and condensation during stage 2, which serve to lock in a particular mesophase.

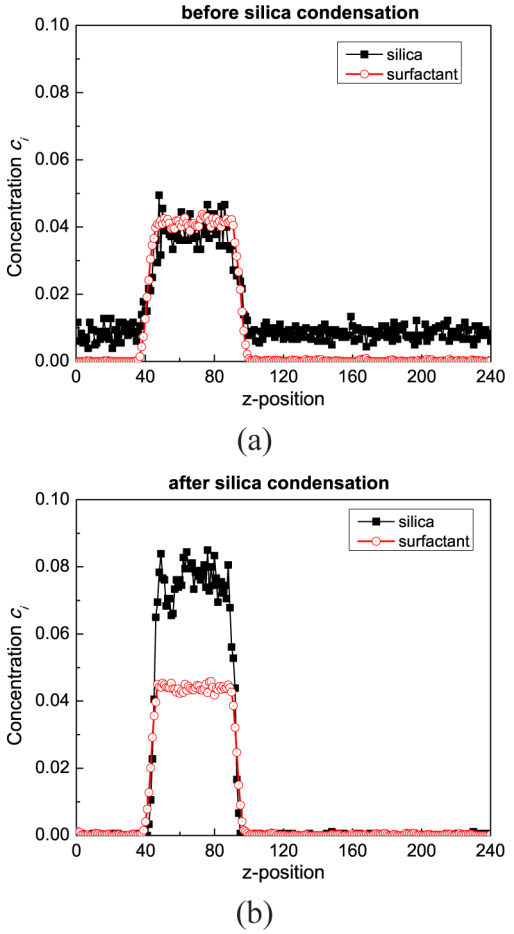

Figure 6. Composition profiles of surfactant−silica−solvent system along the z-axis at T^* = 6.5 (hexagonal phase region) on a 30 × 30 × 240 box with the following concentrations: $c_{H_4T_4}$ = 0.009 375 and c_{Silica} = 0.015. (a) Stage 1 simulations, without silica condensation. (b) Stage 2 simulations, with silica condensation, producing a relatively dense silica−surfactant phase structure.

We have repeated each of our simulations starting from different random number seeds, and we find that the results are reproducible. Now we demonstrate the importance of this two-stage synthesis by simulating a *one-stage* synthesis beginning from the initial condition in Figure 7a, and including all processes from the beginning of the simulation. The result of this is depicted in Figure 7e, showing a more ramified, gel-like silica solid with some short-range silica−surfactant ordering but without the long-range hexagonal order clearly seen in Figure 7c. In particular, the surfactant-rich regions in Figure 7e appear more like spherical micelles than like the cylinders in Figure 7b and c. The material shown in Figure 7e agrees qualitatively with experiments by Beck et al.,[10] who found that MCM-41 synthesis at elevated temperatures, e.g., 200 °C, high enough to activate silica condensation produced only amorphous (and in some cases zeolitic) silica solids. We hypothesize that silica−surfactant solids without long-range order form in the one-stage synthesis because rapid silica polymerization generates glassy materials before surfactant and silica species can reorganize into ordered phases that minimize the system free energy. The two-stage synthesis presumably allows such relaxation in stage 1 to mesophases with long-range order under thermodynamic control.

dx.doi.org/10.1021/la304475j | *Langmuir* 2013, 29, 766−780

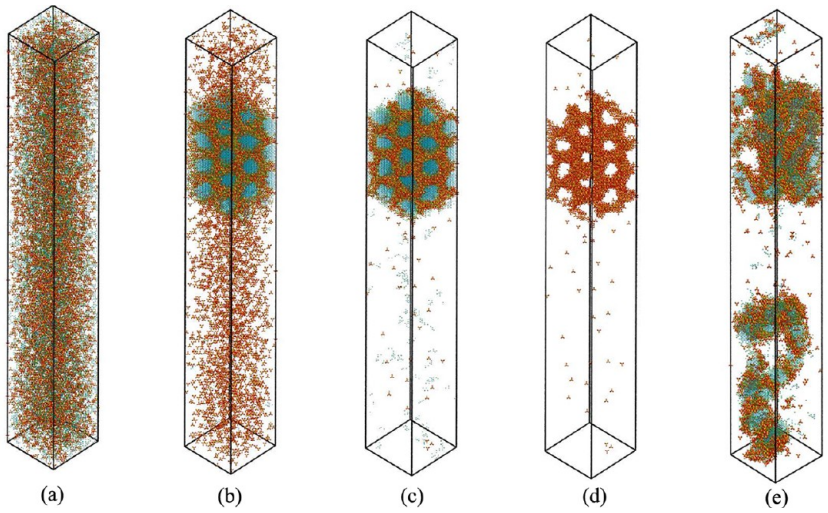

Figure 7. Two-stage synthesis of MCM-41 at $T^* = 6.5$ in a 30 × 30 × 240 box with concentrations $c_{H_4T_4} = 0.009375$ and $c_{Silica} = 0.015$. (a) Initial configuration with 4050 H_4T_4 and 6480 S_I randomly distributed in the simulation cell. (b) Final configuration of stage 1; also initial condition of stage 2. (c) Final configuration of stage 2. (d) Same as (c) except surfactants were omitted to reveal mesopore structure that would arise upon experimental calcination. (e) One-stage synthesis beginning from (a) and with all processes including silica condensation from beginning of simulation; lack of long-range order results from rapid silica polymerization which precludes relaxation to thermodynamic equilibrium surfactant–silica mesophase.

Structural Analysis of the Pore Structures Produced. One of the main objectives in this investigation is to develop and study a model that is simple enough to allow simulated self-assembly of MCM-41, and detailed enough to provide some atomic-level predictions of MCM-41 structure. In this section, we report our structural predictions, focusing on Q_n distributions, ring-size distributions, and pore-size distributions.

Q_n distributions indicate the fractions of silicate species $SiO_n(OH)_{4-n}$ with central Si atoms connected to n bridging oxygens. By definition, silicic acid and its conjugate base are Q_0, Q_1 silica represents dimers and end groups of silica chains, Q_2 corresponds to silica groups in the interior of chains and/or in rings, and Q_3/Q_4 indicate more completely condensed framework structures. During stage 1 of MCM-41 synthesis, most of the silica is presumably Q_0; during stage 2, higher Q_n species become appreciably populated. Q_n distributions are typically measured by ^{29}Si solid-state NMR,[80] which can quantitate different Si environments because of the dipolar nature of the ^{29}Si nucleus.

We have followed the evolution of the Q_n distribution from the end of stage 1 shown in Figure 7b to the end of stage 2 shown in Figure 7c and d, for a system at $T^* = 6.5$ in a 30 × 30 × 240 box with concentrations $c_{H_4T_4} = 0.009\,375$ and $c_{Silica} = 0.015$ (same conditions as in Figure 7). We have plotted the evolution of the Q_n distribution in Figure 8 versus the degree of condensation, $c \equiv \sum_{n=0}^{4} nQ_n/4$, which is the fraction of oxygens that bridge two silicon atoms. The degree of condensation typically increases monotonically with time, and hence serves as a proxy for reaction time. The simulated evolution of the Q_n distribution seen in Figure 8 is characteristic of silica gelation at low pH, where silica polymerization is slow enough to be tracked by NMR.[55,80] In contrast, stage 2 of MCM-41 formation typically occurs experimentally under conditions of rapid silica condensation, thus allowing only measurements of final-state Q_n distributions.

The Q_n distribution from the snapshot in Figure 7d is Q_0:Q_1:Q_2:Q_3:Q_4 = 0.6:4.5:25.6:48.5:20.8. We note that small but significant populations of silica monomers (Q_0) and dimers (Q_1) remain in Figure 7d; these are typically removed in postsynthesis washing/filtration treatments. To better compare our simulations with experiments, we removed the Q_0 and Q_1 populations and recalculated the remaining Q_2:Q_3:Q_4 mole fractions, the results of which are shown in Table 3. Our simulations agree with experiments[11] in the magnitude of $Q_3 \cong 0.5$, the most populated silica species in MCM-41, and in the order of Q_n species: $Q_3 > Q_4 > Q_2$. However, the final Q_4 value in our simulations is about 27% less than that from experiments, likely suggesting that geometrical constraints in the present lattice model make full silica condensation difficult or that the aging process within the silica is not captured on the time scale of our simulations.

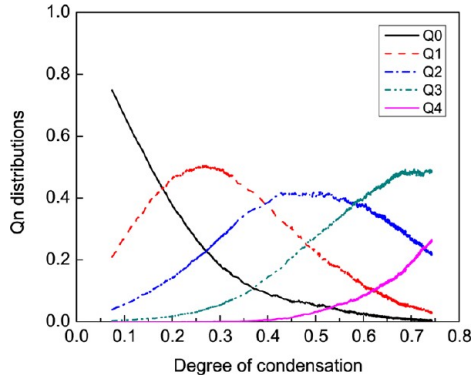

Figure 8. Evolution of Q_n distributions as a function of the degree of condensation, $c \equiv \sum_{n=0}^{4} nQ_n/4$.

Table 3. Q_n Distributions for MCM-41 from Experiments and Simulations

	sur/Si	Q_2	Q_3	Q_4
experiments[11]	0.6	8%	49%	43%
our simulation	0.625	23.2%	49.8%	27.0%

dx.doi.org/10.1021/la304475j | *Langmuir* 2013, 29, 766–780

Ring-size distributions describe structures of crystalline silica such as zeolites,[81] and also provide short- to medium-range information on amorphous silica structure. We have computed the ring-size distribution from the condensed MCM-41 silica in Figure 7c (same silica network in Figure 7d) by counting only irreducible rings, i.e., those that cannot be divided into smaller rings.[79] In general, an *n*-ring refers to a cyclic chain of the form $(Si-O)_n$. Our computed ring-size distribution for MCM-41 is shown in Figure 9 (red circles) plotted alongside our simulated ring-size distribution for amorphous silica gel (blue open squares) computed in previous work with this bcc lattice model.[55] For comparison, we also plot in Figure 9 the ring-size distribution obtained by Kohara and Suzuya from a reverse Monte Carlo fit to high energy X-ray and neutron diffraction data on vitreous silica.[82] Figure 9 shows that, while simulation and "experiment" agree on a relatively sharply peaked ring-size distribution for non-mesoporous amorphous silica, our present simulations on MCM-41 predict a flatter ring-size distribution with larger fractions of 3- and 4-rings. The presence of 3- and 4-rings is consistent with the interpretation by Wakihara et al. of their high energy X-ray diffraction data.[43] The prevalence of such 3- and 4-rings in our simulated MCM-41 is perhaps surprising given the penalties we impose on such rings, suggesting that they are stabilized in our model by proximal surfactants. We have also found higher fractions of larger rings—13-, 14-, and 15-rings—in our simulated MCM-41, consistent with the presence of mesopores.

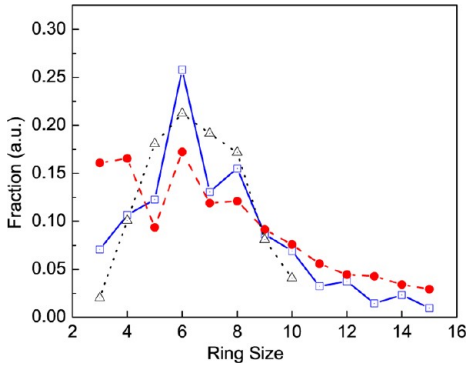

Figure 9. Simulated ring-size distribution of MCM-41 (red circles) for structure in Figure 7c and d, compared with simulated ring-size distribution for silica gel (blue open squares),[55] plotted with ring-size distribution obtained via reverse Monte Carlo fit by Wakihara et al. of high energy diffraction data (black open triangles).[43] These results show an overall flatter distribution in MCM-41 with larger fractions of both small (3-, 4-) rings and large (13-, 14-, 15-) rings.

Next, we consider the pore-size distribution resulting from the MCM-41 shown in Figure 7d. Determining pore sizes is challenging because of molecular scale roughness in the pore walls. Figure 10 shows the corrugation arising in our model, by focusing on the region of Figure 7c rich in surfactant and silica (*z* values between 45 and 90). Figure 10c shows slices through the simulated MCM-41 structure that clearly reveal such roughness. Figure 10c also shows how our simulated mesopores are continued through periodic boundary conditions, by following in the lower plane how surfactant-rich regions continue on the opposite side of the simulation box.

A straightforward approach for determining pore sizes is to fit cylinders into the pores, and to determine the minimum radius of the cylinder that reaches the pore wall for a given pore. However, because of corrugation, this approach generally underestimates pore sizes. An alternative approach proposed by Gelb and Gubbins[83] is to insert spheres at various points in the solid. We have chosen our bcc lattice as a suitable collection of points for inserting spheres. For a given lattice point in the material, spheres of increasing radii were inserted until overlap with one or more of the pore walls was reached; the largest radius that avoids such overlap was then stored. After this procedure was performed for all lattice points, a histogram of diameter was generated, which is shown in Figure 11. We converted the lattice space into physical lengths assuming a silicon–oxygen bond length of 1.6 Å. Figure 11 shows that the average pore size in our simulated MCM-41 corresponds to a pore diameter of around 12 Å, which is reasonably close to the lower bound of pore sizes attainable with MCM-41 materials (~15 Å).[3] The smaller pore size in our simulations can be attributed to the relatively short surfactant chains (H_4T_4) studied herein. In future work, we will investigate how the size and shape of surfactant molecules influence the formation processes and wall morphologies of mesoporous materials.

SUMMARY AND CONCLUSIONS

We have performed Monte Carlo simulations to study the formation and structure of the MCM-41 mesoporous silica solid, building on the modeling work of Siperstein and

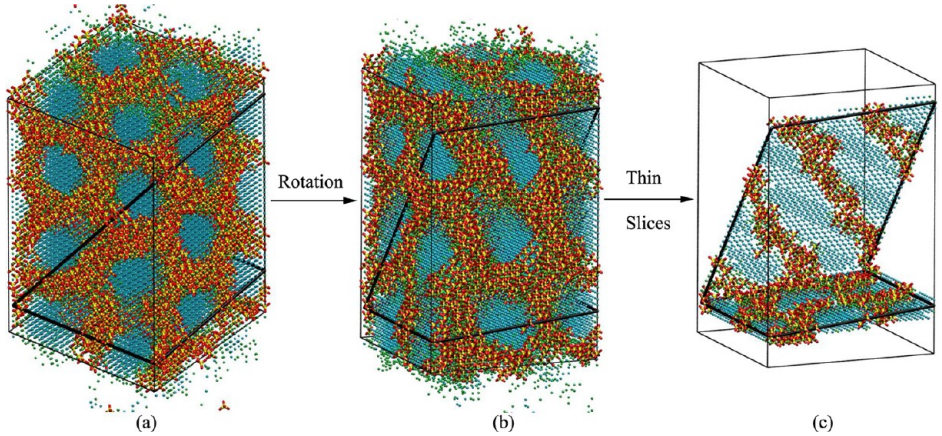

Figure 10. (a) Zoom in on surfactant–silica-rich region of Figure 7c (*z* values between 45 and 90); (b) Rotation of (a); (c) two-dimensional slices from (b) to show mesostructures, pore wall corrugation, and how the mesopores continue through periodic boundary conditions.

dx.doi.org/10.1021/la304475j | *Langmuir* 2013, 29, 766–780

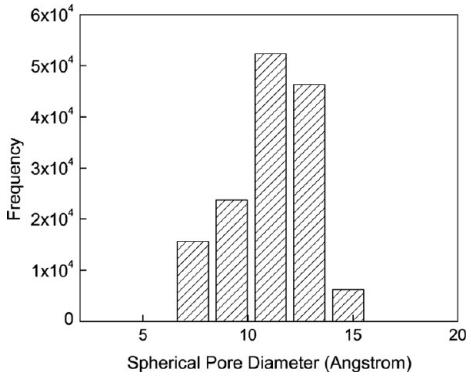

Figure 11. Pore-size distribution of simulated MCM-41 after removing surfactants (structure in Figure 7d), giving an average diameter of 12 Å because of the relatively short H_4T_4 surfactant chains studied herein.

Gubbins.[26] We applied Monte Carlo to sample a new body-centered cubic (bcc) lattice model that explicitly represents both silicic acid polymerization and surfactant self-assembly. Our lattice model of surfactant chains, which was inspired by Larson,[58] involves eight connected particles on a simple-cubic sublattice of the bcc lattice, while our lattice model of silica is an atomic model that represents silicon and oxygen atoms in intact tetrahedra where double occupancy of oxygen sites was used to model silica condensation, following our previous work on silica gel.[55]

We have considered both one-stage and two-stage simulations of MCM-41 self-assembly. In the two-stage simulation, silica−surfactant mesostructures were first allowed to form in the absence of silica polymerization; then, silica polymerization in the second stage served to lock in mesoscale structure. In the one-stage simulation, silica polymerization was allowed from the beginning. We have found that the two-stage approach, i.e., delaying silica polymerization in our simulations, is crucial for generating mesoscale ordering. Our one-stage simulations produced silica−surfactant gels with little to no order, in agreement with experiments.[10] Our two-stage simulations produced silica−surfactant mesostructures with lamellar or hexagonal phases. Before silica polymerization, we observed reversible transformations between these lamellar and hexagonal phases, also in agreement with experiment.[14] Our results are consistent with the cooperative templating mechanism, because silica−surfactant complexes were prominent at the earliest stages of our simulations.

The MCM-41 solid that results from our simulations exhibits Q_n distributions in reasonable agreement with ^{29}Si NMR experiments on MCM-41. Compared with amorphous silica gel, the wall domains of these simulated MCM-41 materials were found to exhibit broader ring-size distributions including larger fractions of smaller (3-, 4-) rings and larger (13-, 14-, 15-) rings. The presence of smaller rings in MCM-41 is consistent with high energy diffraction studies, and the larger rings are expected in a mesoporous solid.

Our work has provided a model that is simple enough to allow simulations of the self-assembly of MCM-41 and detailed enough to provide atomic-level predictions of MCM-41 structure. We will extend this to study the influence of surfactant size and shape on material formation and resulting structure. We will also investigate other mesopore morphologies and how they form. It will also be interesting to make more detailed structural characterizations and studies of the adsorption properties of the model materials emerging from these studies. The progress represented by our model comes at the cost of making several assumptions/simplifications, the consequences of which will need to be explored in future work. These include the assumption of complete ion exchange between the surfactant and silicate anions and the presence of silica oligomers in the system prior to mesophase formation.

AUTHOR INFORMATION

Corresponding Author

*E-mail: auerbach@chem.umass.edu (S.M.A.); monson@ecs.umass.edu (P.A.M.).

Notes

The authors declare no competing financial interest.

ACKNOWLEDGMENTS

This work was supported by a grant from the U.S. Department of Energy (Contract No. DE-FG02-07ER46466). The authors thank Professor Wei Fan for stimulating discussions on mesoporous silica materials.

REFERENCES

(1) Yanagisawa, T.; Shimizu, T.; Kuroda, K.; Kato, C. The preparation of alkyltrimethylammonium-kanemite complexes and their conversion to microporous materials. *Bull. Chem. Soc. Jpn.* **1990**, *63*, 988−992.

(2) Kresge, C. T.; Leonowicz, M. E.; Roth, W. J.; Vartuli, J. C.; Beck, J. S. Ordered mesoporous molecular-sieves synthesized by a liquid-crystal template mechanism. *Nature* **1992**, *359*, 710−712.

(3) Beck, J. S.; Vartuli, J. C.; Roth, W. J.; Leonowicz, M. E.; Kresge, C. T.; Schmitt, K. D.; Chu, C. T. W.; Olson, D. H.; Sheppard, E. W.; Mccullen, S. B.; Higgins, J. B.; Schlenker, J. L. A new family of mesoporous molecular-sieves prepared with liquid-crystal templates. *J. Am. Chem. Soc.* **1992**, *114*, 10834−10843.

(4) Hartmann, M. Ordered mesoporous materials for bioadsorption and biocatalysis. *Chem. Mater.* **2005**, *17*, 4577−4593.

(5) Wang, S. Ordered mesoporous materials for drug delivery. *Microporous Mesoporous Mater.* **2009**, *117*, 1−9.

(6) Manzano, M.; Vallet-Regi, M. New developments in ordered mesoporous materials for drug delivery. *J. Mater. Chem.* **2010**, *20*, 5593−5604.

(7) Monnier, A.; Schuth, F.; Huo, Q.; Kumar, D.; Margolese, D.; Maxwell, R. S.; Stucky, G. D.; Krishnamurty, M.; Petroff, P.; Firouzi, A.; Janicke, M.; Chmelka, B. F. Cooperative formation of inorganic-organic interfaces in the synthesis of silicate mesostructures. *Science* **1993**, *261*, 1299−1303.

(8) Chen, C. Y.; Li, H. X.; Davis, M. E. Studies on mesoporous materials. I. Synthesis and characterization of MCM-41. *Microporous Mater.* **1993**, *2*, 17−26.

(9) Chen, C. Y.; Burkett, S. L.; Li, H. X.; Davis, M. E. Studies on mesoporous materials. II. Synthesis mechanism MCM-41. *Microporous Mater.* **1993**, *2*, 27−34.

(10) Beck, J. S.; Vartuli, J. C.; Kennedy, G. J.; Kresge, C. T.; Roth, W. J.; Schramm, S. E. Molecular or supramolecular templating: Defining the role of surfactant chemistry in the formation of microporous and mesoporous molecular sieves. *Chem. Mater.* **1994**, *6*, 1816−1821.

(11) Vartuli, J. C.; Schmitt, K. D.; Kresge, C. T.; Roth, W. J.; Leonowicz, M. E.; McCullen, S. B.; Hellring, S. D.; Beck, J. S.; Schlenker, J. L.; Olson, D. H.; Sheppard, E. W. Effect of surfactant/silica molar ratios on the formation of mesoporous molecular sieves: Inorganic mimicry of surfactant liquid-crystal phases and mechanistic implications. *Chem. Mater.* **1994**, *6*, 2317−2326.

(12) Firouzi, A.; Kumar, D.; Bull, L. M.; Besier, T.; Sieger, P.; Huo, Q.; Walker, S. A.; Zasadzinski, J. A.; Glinka, C.; Nicol, J.; Margolese, D.; Stucky, G. D.; Chmelka, B. F. Cooperative organization of inorganic-surfactant and biomimetic assemblies. *Science* **1995**, *267*, 1138−1143.

(13) Attard, G. S.; Glyde, J. C.; G., G. C. Liquid-crystalline phases as templates for the synthesis of mesoporous silica. *Nature* **1995**, *378*, 366−368.
(14) Firouzi, A.; Atef, F.; Oertli, A. G.; Stucky, G. D.; Chmelka, B. F. Alkaline lyotropic silicate-surfactant liquid crystals. *J. Am. Chem. Soc.* **1997**, *119*, 3596−3610.
(15) Corma, A. From microporous to mesoporous molecular sieve materials and their use in catalysis. *Chem. Rev.* **1997**, *97*, 2373−2419.
(16) Zhao, D. Y.; Feng, J. L.; Huo, Q. S.; Melosh, N.; Fredrickson, G. H.; Chmelka, B. F.; Stucky, G. D. Triblock copolymer syntheses of mesoporous silica with periodic 50 to 300 angstrom pores. *Science* **1998**, *279*, 548−552.
(17) Zhao, D. Y.; Huo, Q. S.; Feng, J. L.; Chmelka, B. F.; Stucky, G. D. Nonionic triblock and star diblock copolymer and oligomeric surfactant syntheses of highly ordered, hydrothermally stable, mesoporous silica structures. *J. Am. Chem. Soc.* **1998**, *120*, 6024−6036.
(18) Yang, P. D.; Zhao, D. Y.; Chmelka, B. F.; Stucky, G. D. Triblock-copolymer-directed syntheses of large-pore mesoporous silica fibers. *Chem. Mater.* **1998**, *10*, 2033−2036.
(19) Davis, M. E. Ordered porous materials for emerging applications. *Nature* **2002**, *417*, 813−821.
(20) Lin, H. P.; Mou, C. Y. Structural and morphological control of cationic surfactant-templated mesoporous silica. *Acc. Chem. Res.* **2002**, *35*, 927−935.
(21) Fedeyko, J. M.; Vlachos, D. G.; Lobo, R. F. Understanding the differences between microporous and mesoporous synthesis through the phase behavior of silica. *Microporous Mesoporous Mater.* **2006**, *90*, 102−111.
(22) Beurroies, I.; Agren, P.; Buechel, G.; Rosenholm, J. B.; Amenitsch, H.; Denoyel, R.; Linden, M. Detailed in situ XRD and calorimetric study of the formation of silicate/mixed surfactant mesophases under alkaline conditions. Influence of surfactant chain length and synthesis temperature. *J. Phys. Chem. B* **2006**, *110*, 16254−16260.
(23) Huo, Q. S.; Margolese, D. I.; Ciesla, U.; Demuth, D. G.; Feng, P. Y.; Gier, T. E.; Sieger, P.; Firouzi, A.; Chmelka, B. F.; Schuth, F.; Stucky, G. D. Organization of organic molecules with inorganic molecular species into nanocomposite biphase arrays. *Chem. Mater.* **1994**, *6*, 1176−1191.
(24) Raman, N. K.; Anderson, M. T.; Brinker, C. J. Template-based approaches to the preparation of amorphous, nanoporous silicas. *Chem. Mater.* **1996**, *8*, 1682−1701.
(25) Siperstein, F. R.; Gubbins, K. E. Synthesis and characterization of templated mesoporous materials using molecular simulation. *Mol. Simul.* **2001**, *27*, 339−352.
(26) Siperstein, F. R.; Gubbins, K. E. Phase separation and liquid crystal self-assembly in surfactant-inorganic-solvent systems. *Langmuir* **2003**, *19*, 2049−2057.
(27) Smith, W. R.; Triska, B. The reaction ensemble method for the computer-simulation of chemical and phase-equilibria 0.1. Theory and basic examples. *J. Chem. Phys.* **1994**, *1 00*, 3019−3027.
(28) Johnson, J. K.; Panagiotopoulos, A. Z.; Gubbins, K. E. Reactive canonical Monte-Carlo - a new simulation technique for reacting or associating fluids. *Mol. Phys.* **1994**, *81*, 717−733.
(29) Zhang, J. Y.; Luz, Z.; Goldfarb, D. EPR studies of the formation mechanism of the mesoporous materials MCM-41 and MCM-50. *J. Phys. Chem. B* **1997**, *101*, 7087−7094.
(30) Linden, M.; Schunk, S. A.; Schuth, F. In situ X-ray diffraction study of the initial stages of formation of MCM-41 in a tubular reactor. *Angew. Chem., Int. Ed.* **1998**, *37*, 821−823.
(31) Agren, P.; Linden, M.; Rosenholm, J. B.; Schwarzenbacher, R.; Kriechbaum, M.; Amenitsch, H.; Laggner, P.; Blanchard, J.; Schuth, F. Kinetics of cosurfactant-surfactant-silicate phase behavior. 1. Short-chain alcohols. *J. Phys. Chem. B* **1999**, *103*, 5943−5948.
(32) Regev, O. Nucleation events during the synthesis of mesoporous materials using liquid crystalline templating. *Langmuir* **1996**, *12*, 4940−4944.
(33) Lee, Y. S.; Surjadi, D.; Rathman, J. F. Effects of aluminate and silicate on the structure of quaternary ammonium surfactant aggregates. *Langmuir* **1996**, *12*, 6202−6210.
(34) Galarneau, A.; Di Renzo, F.; Fajula, F.; Mollo, L.; Fubini, B.; Ottaviani, M. F. Kinetics of formation of micelle-templated silica mesophases monitored by electron paramagnetic resonance. *J. Colloid Interface Sci.* **1998**, *201*, 105−117.
(35) Albuquerque, A.; Vautier-Giongo, C.; Pastore, H. Physical chemistry of nanostructured molecular sieves by the study of phase diagrams: the case of the cetyltrimethylammonium bromide-tetramethylammonium silicate-water system. *J. Colloid Interface Sci.* **2005**, *284*, 687−693.
(36) Sadasivan, S.; Fowler, C.; Khushalani, D.; Mann, S. Nucleation of MCM-41 nanoparticles by internal reorganization of disordered and nematic-like silica surfactant clusters. *Angew. Chem., Int. Ed.* **2002**, *41*, 2151−2153.
(37) Zana, R.; Frasch, J.; Soulard, M.; Lebeau, B.; Patarin, J. Fluorescence probing investigations of the mechanism of formation of organized mesoporous silica. *Langmuir* **1999**, *15*, 2603−2606.
(38) Frasch, J.; Lebeau, B.; Soulard, M.; Patarin, J.; Zana, R. In situ investigations on cetyltrimethyl ammonium surfactant/silicate systems, precursors of organized mesoporous MCM-41-type siliceous materials. *Langmuir* **2000**, *16*, 9049−9057.
(39) Vautier-Giongo, C.; Pastore, H. O. Micellization of CTAB in the presence of silicate anions and the exchange between bromide and silicate at the micelle surface: A step to understand the formation of mesoporous molecular sieves at extremely low surfactant and silicate concentrations. *J. Colloid Interface Sci.* **2006**, *299*, 874−882.
(40) Baute, D.; Frydman, V.; Zimmermann, H.; Kababya, S.; Goldfarb, D. Properties of the silica layer during the formation of MCM-41 studied by EPR of a silica-bound spin probe. *J. Phys. Chem. B* **2005**, *109*, 7807−7816.
(41) de Man, A. J. M.; Ueda, S.; Annen, M. J.; Davis, M. E.; van Santen, R. A. The stability and vibrational-spectra of 3-ring containing zeolitic silica polymorphs. *Zeolites* **1992**, *12*, 789−800.
(42) Annen, M. J.; Davis, M. E. Raman and ^{29}Si MAS NMR spectroscopy of framework materials containing three-membered rings. *Microporous Mater.* **1993**, *1*, 57−65.
(43) Wakihara, T.; Fan, W.; Kohara, S.; Ogura, M.; Sankar, G.; Okubo, T. Intermediate-range order in mesoporous silicas investigated by a high-energy x-ray diffraction technique. *Chem. Lett.* **2008**, *37*, 30−31.
(44) Patti, A.; Mackie, A. D.; Siperstein, F. R. Monte Carlo simulation of self-assembled ordered hybrid materials. *Langmuir* **2007**, *23*, 6771−6780.
(45) Patti, A.; Siperstein, F. R.; Mackie, A. D. Phase behavior of model surfactants in the presence of hybrid particles. *J. Phys. Chem. C* **2007**, *111*, 16035−16044.
(46) Patti, A.; Mackie, A. D.; Zelenak, V.; Siperstein, F. R. One-pot synthesis of amino functionalized mesoporous silica materials: using simulations to understand transitions between different structures. *J. Mater. Chem.* **2009**, *19*, 724−732.
(47) Patti, A.; Mackie, A. D.; Siperstein, F. R. Monte Carlo simulations of self-assembling hexagonal and cage-like bifunctional periodic mesoporous materials. *J. Mater. Chem.* **2009**, *19*, 7848−7855.
(48) Schumacher, C.; Gonzalez, J.; Wright, P. A.; Seaton, N. A. Generation of atomistic models of periodic mesoporous silica by kinetic Monte Carlo simulation of the synthesis of the material. *J. Phys. Chem. B* **2006**, *110*, 319−333.
(49) Jorge, M.; Gomes, J. R. B.; Natalia, M.; Cordeiro, D. S.; Seaton, N. A. Molecular simulation of silica/surfactant self-assembly in the synthesis of periodic mesoporous silicas. *J. Am. Chem. Soc.* **2007**, *129*, 15414−15415.
(50) Jorge, M.; Gomes, J. R. B.; Cordeiro, M. N. D. S.; Seaton, N. A. Molecular dynamics simulation of the early stages of the synthesis of periodic mesoporous silica. *J. Phys. Chem. B* **2009**, *113*, 708−718.
(51) Jorge, M.; Auerbach, S. M.; Monson, P. A. Modeling spontaneous formation of precursor nanoparticles in clear-solution zeolite synthesis. *J. Am. Chem. Soc.* **2005**, *127*, 14388−14400.

(52) Jorge, M.; Auerbach, S. M.; Monson, P. A. Modelling the thermal stability of precursor nanoparticles in zeolite synthesis. *Mol. Phys.* **2006**, *104*, 3513−3522.
(53) Jin, L.; Auerbach, S. M.; Monson, P. A. Modeling nanoparticle formation during early stages of zeolite growth: a low-coordination lattice model of template penetration. *J. Phys. Chem. C* **2010**, *114*, 14393−14401.
(54) Jin, L.; Auerbach, S. M.; Monson, P. A. Emergence of zeolite analogs and other microporous crystals in an atomic lattice model of silica and related materials. *J. Phys. Chem. Lett.* **2012**, *3*, 761−765.
(55) Jin, L.; Auerbach, S. M.; Monson, P. A. Modeling three-dimensional network formation with an atomic lattice model: Application to silicic acid polymerization. *J. Chem. Phys.* **2011**, *134*, 134703.
(56) Leontidis, E. Hofmeister anion effects on surfactant self-assembly and the formation of mesoporous solids. *Curr. Opin. Colloid Interface Sci.* **2002**, *7*, 81−91.
(57) Kittel, C. *Introduction to Solid State Physics*; Wiley: New York, 1996.
(58) Larson, R. G.; Scriven, L. E.; Davis, H. T. Monte-Carlo simulation of model amphiphilic oil-water systems. *J. Chem. Phys.* **1985**, *83*, 2411−2420.
(59) Larson, R. G. Self-assembly of surfactant liquid-crystalline phases by Monte-Carlo simulation. *J. Chem. Phys.* **1989**, *91*, 2479−2488.
(60) Larson, R. G. Monte-Carlo simulation of microstructural transitions in surfactant systems. *J. Chem. Phys.* **1992**, *96*, 7904−7918.
(61) Larson, R. G. Monte Carlo simulations of the phase behavior of surfactant solutions. *J. Phys. II* **1996**, *6*, 1441−1463.
(62) Floriano, M. A.; Caponetti, E.; Panagiotopoulos, A. Z. Micellization in model surfactant systems. *Langmuir* **1999**, *15*, 3143−3151.
(63) Sefcik, J.; McCormick, A. V. Thermochemistry of aqueous silicate solution precursors to ceramics. *AIChE J.* **1997**, *43*, 2773−2784 (AIChE Topical Conference on Advanced Ceramics Processing as Part of the 5th World Congress of Chemical Engineering, San Diego, CA, July, 1996).
(64) White, C. E.; Provis, J. L.; Kearley, G. J.; Riley, D. P.; van Deventer, J. S. J. Density functional modelling of silicate and aluminosilicate dimerisation solution chemistry. *Dalton Trans.* **2011**, *40*, 1348−1355.
(65) Mackie, A. D.; Onur, K.; Panagiotopoulos, A. Z. Phase equilibria of a lattice model for an oil-water-amphiphile mixture. *J. Chem. Phys.* **1996**, *104*, 3718−3725.
(66) Mackie, A. D.; Panagiotopoulos, A. Z.; Szleifer, I. Aggregation behavior of a lattice model for amphiphiles. *Langmuir* **1997**, *13*, 5022−5031.
(67) Wright, J. D.; Sommerdijk, N. A. J. M. *Sol-Gel Materials: Chemistry and Applications*; Gordon and Breach Science: Amsterdam, The Netherlands, 2001.
(68) Fernandez-Cata, G.; Perez-Gramatges, A.; Javier Alvarez, L.; Comas-Rojas, H.; Zicovich-Wilson, C. M. On the interaction between silica surfaces and surfactants. A 2D periodic B3LYP investigation. *J. Phys. Chem. C* **2009**, *113*, 13309−13316.
(69) Rosenbluth, M. N.; Rosenbluth, A. W. Monte-Carlo calculation of the average extension of molecular chains. *J. Chem. Phys.* **1955**, *23*, 356−359.
(70) Siepmann, J. I.; Frenkel, D. Configurational bias Monte-Carlo - a new sampling scheme for flexible chains. *Mol. Phys.* **1992**, *75*, 59−70.
(71) Frenkel, D.; Smit, B. *Understanding Molecular Simulation: From Algorithms to Applications*, 2nd ed.; Academic Press: San Diego, CA, 1996.
(72) Swendsen, R. H.; Wang, J. S. Nonuniversal critical-dynamics in Monte-Carlo simulations. *Phys. Rev. Lett.* **1987**, *58*, 86−88.
(73) Wu, D.; Chandler, D.; Smit, B. Electrostatic analogy for surfactant assemblies. *J. Phys. Chem.* **1992**, *96*, 4077−4083.
(74) Iler, R. K. *The Chemistry of Silica: Solubility, Polymerization, Colloid and Surface Properties and Biochemistry*; Wiley: New York, 1979.
(75) White, C. E.; Provis, J. L.; Proffen, T.; van Deventer, J. S. J. Quantitative mechanistic modeling of silica solubility and precipitation during the initial period of zeolite synthesis. *J. Phys. Chem. C* **2011**, *115*, 9879−9888.
(76) Rimer, J. D.; Lobo, R. F.; Vlachos, D. G. Physical basis for the formation and stability of silica nanoparticles in basic solutions of monovalent cations. *Langmuir* **2005**, *21*, 8960−8971.
(77) Brinker, C. J. Hydrolysis and condensation of silicates: Effects on structure. *J. Non-Cryst. Solids* **1988**, *100*, 31−50.
(78) Hoshen, J.; Kopelman, R. Percolation and cluster distribution 0.1. Cluster multiple labeling technique and critical concentration algorithm. *Phys. Rev. B* **1976**, *14*, 3438−3445.
(79) Yuan, X. L.; Cormack, A. N. Efficient algorithm for primitive ring statistics in topological networks. *Comput. Mater. Sci.* **2002**, *24*, 343−360.
(80) Malier, L.; Boilot, J. P.; Chaput, F.; Devreus, F. NMR-study of silica gelation kinetics. *Phys. Rev. A* **1992**, *46*, 959−962.
(81) Lobo, R. F. In *Handbook of zeolite science and technology*; Auerbach, S. M., Carrado, K. A., Dutta, P. K., Eds.; Dekker Inc.: New York, 2003; pp 65−128.
(82) Kohara, S.; Suzuya, K. Intermediate-range order in Vitreous SiO2 and GeO2. *J. Phys.: Condens. Matter* **2005**, *17*, S77−S86.
(83) Gelb, L. D.; Gubbins, K. E. Pore size distributions in porous glasses: A computer simulation study. *Langmuir* **1999**, *15*, 305−308.